

Spectroscopic Analysis of Quantum Spin Liquids and Nanophotonic Cavities

Yoong Sheng Phang,^{1, a)} Brian Lerner,² Yun-Yi Pai,² Vasudevan Iyer,² Benjamin J. Lawrie,^{2, b)} and Thang Ba Hoang³

¹⁾*University of Georgia, Athens, GA 30602*

²⁾*Oak Ridge National Laboratory, Oak Ridge, TN 37831*

³⁾*University of Memphis, Memphis, TN 38152*

(Dated: 29 April 2021)

The spectroscopy of quantum materials and plasmonic heterostructures produces multidimensional and hyperspectral datasets containing information about the magnetic, electronic, and optical properties of a sample. To extract trends in such datasets accurately and efficiently, the exploration of different spectral analysis techniques as well as a robust framework for image processing and visualization are necessary. In this project, we explore datasets acquired from two classes of materials: quantum spin liquids (QSL) and nanophotonic cavities. First, we experiment with spectral unmixing by nonnegative matrix factorization (NMF) on the temperature, field, and polarization resolved Raman spectra of the QSL candidate α -RuCl₃. NMF is extended to a spatially resolved cathodoluminescence (CL) microscopy dataset for an Ag nanocube on gold thin-film. Additionally, we develop a Python panel to visualize the localized and propagating plasmon modes in this heterostructure. Preliminary efforts toward enhancing the quality of hyperspectral CL images by pan sharpening are underway.

I. INTRODUCTION

Recent advancements in spectroscopic methods have provided increased insight into the magnetic, electronic, and optical properties of quantum materials and plasmonic heterostructures. The data acquired from spectroscopy on these materials is oftentimes presented in the form of a multidimensional dataset or a hyperspectral data cube. To extract the underlying information about the physical properties of a material from such datasets, a variety of Bayesian and frequentist regression methods as well as spectral unmixing methods such as principal component analysis (PCA), k-means clustering, singular value decomposition (SVD), and nonnegative matrix factorization (NMF) are being explored for analysis. Equally important is the need to find an efficient way to visualize these datasets. Ongoing efforts such as Oak Ridge National Laboratory's pyCrospec package, seek to develop a universal framework for processing and visualizing spectral data.^{1,2} Recently, pan-sharpening, which is traditionally used in geospatial applications,³ has been applied to enhance hyperspectral imaging of materials.

In this paper, we demonstrate the spectral unmixing by NMF on multidimensional Raman spectra of the candidate Quantum Spin Liquid α -RuCl₃ and expand this technique to hyperspectral data acquired by spatially resolved cathodoluminescence (CL) microscopy of an Ag nanopatch antenna. We also develop a Python application to allow the user to easily visualize plasmon modes in plasmonic heterostructures and apply it to the hyperspectral CL dataset.

II. EXPERIMENTAL METHODS

A. Raman Spectroscopy

Raman spectroscopy is a particularly useful tool for investigating QSL's because it can probe magnon-phonon and phonon-spinon coupling and resolve sample symmetry. Magnetic field, temperature, and polarization resolved multidimensional datasets were obtained by Raman spectroscopy on the candidate QSL RuCl₃. The out-of-plane magnetic field was swept from $B = 0$ T to $B = +6$ T to $B = -6$ T to $B = 0$ in 1 T increments. Measurements were acquired at $T = 670$ mK and $T = 4$ K. Polarization was varied from 0 to 360 degrees. The resulting data is returned in .asc files, which must be processed for the purposes of computational analysis.

B. Cathodoluminescence Microscopy

CL microscopy directly probes the radiative local density of optical states by using a beam of electrons as a broadband source of optical excitation,⁴ and is an effective technique for studying the near-field optical properties of plasmonic heterostructures. Here, we use spatially and spectrally resolved CL microscopy to map the amplitude and phase of localized and propagating surface plasmons. All samples were excited with an electron beam energy of 30 keV, and beam currents between 630 and 5600 pA. Spectra were acquired with dwell times of 0.2-2 s per pixel, and spectrum images. Reference images were taken for drift correction every 2-20 s. The data is stored as a hyperspectral data cube in hdf5 files.

C. Scanning Electron Microscopy

In scanning tunneling electron microscopy (STEM), a focused electron beam is swept over a material surface. The

^{a)}Electronic mail: ysp79161@uga.edu

^{b)}Electronic mail: lawrie@ornl.gov

signal from interactions between the electrons and the sample are collected to form an image that provide information about its surface topography and composition. During CL imaging, an SEM image is produced as a byproduct of sweeping the focused electron beam across the sample. The SEM image can be used alongside CL images as a reference to study correlations between material morphology and the dynamics of the material. Here, the secondary electron emission signal is collected to form the SEM image.

III. COMPUTATIONAL METHODS

A. Nonnegative Matrix Factorization

Nonnegative Matrix factorization (NMF) is a method of spectral unmixing used to analyze high-dimensional data by extracting sparse and meaningful features from a set of non-negative data vectors.⁵ Given a matrix of collected spectral data Y of dimension $n \times m$, it is assumed that the data contains an approximately linear mixture of underlying components, and that the data is nonnegative.⁶ Thus, Y can be decomposed as,

$$Y \approx WH \quad (1)$$

Where the nonnegative matrices W and H have dimensions $n \times r$ and $r \times m$, respectively. This is accomplished by minimizing the squared reconstruction error $\|Y - WH\|^2$.⁷ In this work, NMF is applied in two contexts: (1) to analyze the multidimensional Raman spectra of QSL's, and (2) to analyze hyperspectral CL datasets on plasmonic heterostructures. For the Raman spectra, NMF can identify r components which allow for the recovery of all m measurements by composition according to respective contributions. The spectral endmembers are given by the columns of W . Each endmember has a corresponding relative abundance that is contained in the columns of H .⁸ This concept is the same for the hyperspectral CL data. However, since the data is presented in the form of a hyperspectral data cube, the data must be flattened before performing NMF and subsequently resized to obtain the endmembers and abundance maps.⁹

B. Analysis Tools

Holoviews, an open-source Python library, was used for data visualization and was used in conjunction with the Panels package to develop a user interface for processing and analyzing CL data. Because experimental data from Raman spectroscopy was provided in the form of .asc files and the hyperspectral CL data was provided as .hdf5 files, we unpacked and processed the data before re-packing it into Python xArrays, which allowed us to label the coordinates, dimensions, attributes, and other metadata for easy of access. In some cases, further packaging of these xArrays into netCDF files provided an added degree of accessibility. Sci-kit learn, a Python machine learning library, was used to perform spectral

unmixing by NMF and related analyses. Finally, the Python Panels package was used to develop the user interface for visualization of hyperspectral CL data.

IV. RESULTS

A. Candidate Quantum Spin Liquid α -RuCl₃

QSL's are a system of spins characterized by a topological order parameter. In QSL's, strong quantum fluctuations and the frustration of spin configurations prevent long range order from being established, even at very low or zero temperatures.¹⁰ However, they are also highly correlated through mutual interactions like long-range entanglement and associated fractional spin excitations.¹¹ α -RuCl₃ is a candidate QSL with a honeycomb lattice structure (Fig. 1 inset). α -RuCl₃ has been described extensively from a theoretical standpoint by the analytically solvable Kitaev model.¹² Experimental efforts are also underway to identify a QSL phase in α -RuCl₃. In this section, we conduct exploratory data analysis on the Raman spectra of α -RuCl₃ flakes and detail several interesting observations in the datasets.

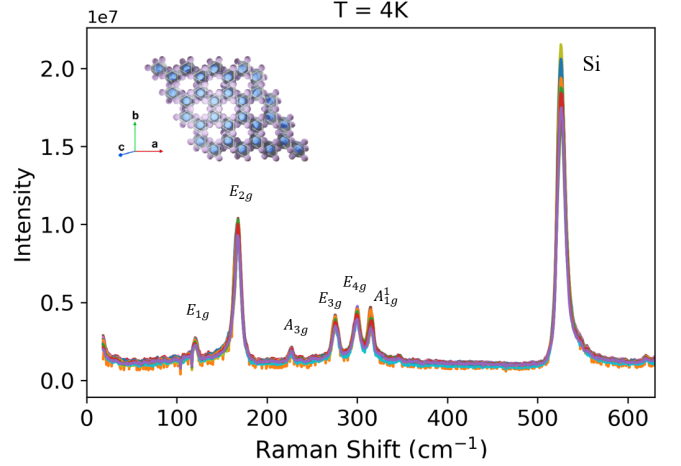


FIG. 1. α -RuCl₃ Stokes side Raman modes at $T = 4\text{K}$. Modes are labeled according to the $R\bar{3}$ space group. The structure of α -RuCl₃ is inset.

We assign the peaks in the Raman spectrum shown in Fig. 1 according to the rhombohedral $R\bar{3}$ space group, which could possibly describe the low temperature symmetry of α -RuCl₃ according to early literature.^{13,14} We identify E_g^1 at 116 cm^{-1} , E_g^2 at 164 cm^{-1} , E_g^3 at 272 cm^{-1} , and E_g^4 at 296 cm^{-1} . The peaks at 222 cm^{-1} and 345 cm^{-1} are less reported in literature. The former has been attributed to stacking faults or defects, while the latter, whose width has a field dependence, has been attributed to defects and A_{1g}^1 due to its XX polarization.

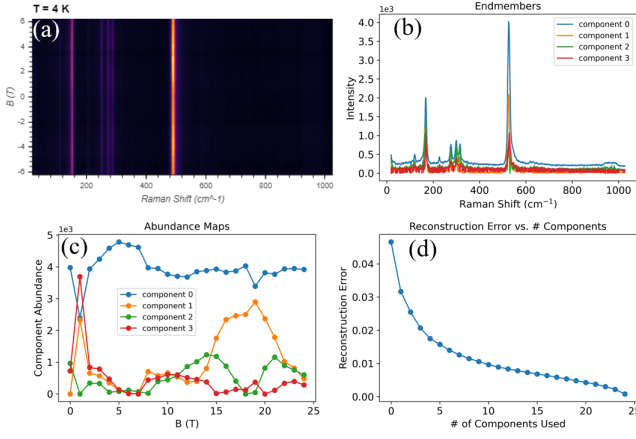


FIG. 2. (a) Raman spectrum at each field taken at $T = 4$ K for each magnetic field B ; (b) endmembers and (c) abundance maps of Raman spectrum after application of NMF; (d) decrease in reconstruction error with increasing number of NMF components

We performed NMF on the multidimensional Raman datasets acquired from α -RuCl₃. First, the data was stored in a Python xArray, so that it could be easily accessed by referencing its metadata. A library of NMF functions was written, which took xArrays as input and returned the results of the spectral unmixing. An open research question regarding NMF is the determination of the number of components to use in the decomposition *a priori*. To determine the number of components, we take a simplified approach by studying the behavior of the reconstruction error. By performing NMF with components from $n = 1$ to $n = 25$, and plotting the reconstruction error against number of components, we find a diminishing return in the reconstruction error, with less significant changes in reconstruction error after $n = 4$ components. Furthermore, we observed that noise-dominated endmembers were introduced to the NMF decomposition for component numbers greater than $n = 4$. Thus, we choose $n = 4$ as our component number for NMF. Based on the component weights shown in Fig. 2(c), the first component is the most representative of the Raman Y matrix across all magnetic fields.

Previous reports have suggested that the Raman scattering continuum can reveal features that are consistent with a QSL phase.^{15,16} We conducted a brief investigation of the baseline by extracting it using the Asymmetric Least Squares algorithm reported by He et al¹⁷ and performing standard frequentist fits of the scattering continuum using combinations of Gaussian, Lorentzian, and Fano curves. While the behavior of the fit parameters as a function of field behaves as expected, deeper methods such as Bayesian regression may be necessary to extract significant information about the scattering interactions.

B. Ag Nanopatch Antenna

Plasmonic nanopatch antennas with dielectric gaps hundreds of picometers to several nanometers thick have drawn increasing attention due to their ability to confine electromag-

netic fields to grossly sub-diffraction limited volumes. Many studies have simulated the near-field optical response of plasmonic cavities, but in practice, inhomogeneities in the devices can constrain the photonic response. In this section, we investigate the near-field interactions in an Ag nanopatch antenna by mapping localized and propagating plasmon modes in experimental CL datasets.

We studied the spatially resolved CL of an Ag nanopatch antenna (SEM image inset in Fig. 3). In this heterostructure, an Au thin film is deposited on a Si/glass substrate. A ZnO spacer layer above the Au film is covered in CdSe quantum dots, upon which rests an Ag nanocube. CL microscopy on the sample yields an hdf5 data file that was processed before analysis by extracting image information (i.e. pixel dimensions of the CL images, wavelength arrays, and scaling factors) from the metadata and applying a spike correction with the Delmic Odemis software. To improve the visibility of the CL images, the spectrum of pixels far from the Ag nanocube are averaged together and subtracted from the hyperspectral datacube as a background spectrum. The datacube, x and y coordinates, and wavelengths are packaged into xArray format for analysis.

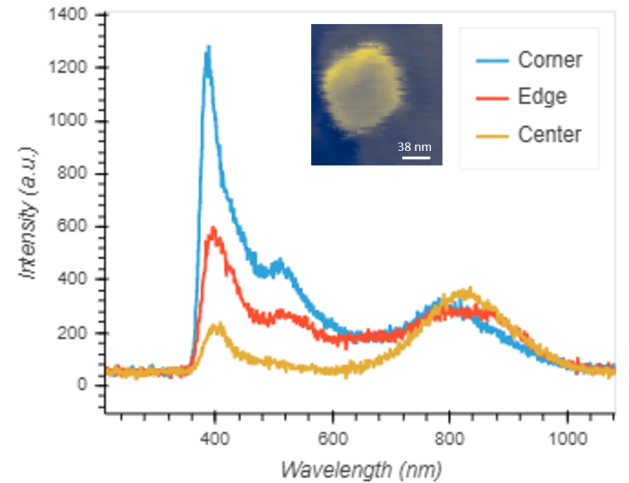


FIG. 3. Spectra taken at the center, corner, and edge of the Ag nanocube with SEM image inset

The Ag nanocube contains three distinct plasmon modes, centered at wavelengths of 400 nm, 520 nm, and 820 nm as shown in Fig. 4. To visualize these plasmon modes in spatial coordinates, we developed an interactive hyperspectral visualizer (IHV) tool for plasmonic heterostructures. Briefly, the IHV allows the user to dynamically visualize plasmon modes by interacting with a Python panel interface to adjust the wavelength range, bandwidth, intensity scale, color scheme, and figure formatting. The IHV operates by using the xArray containing the background subtracted hyperspectral CL data as inputs to four classes: `BaseModeViewer`, `ModeViewer`. The parameterized class `BaseModeViewer` creates a panel for visualizing the background subtracted dataset, and `ModeViewer` inherits each of its properties to generate a layout of spectral images that takes the aforemen-

tioned filtering parameters as input. **ModeViewer** is inherited by two distinct classes: **PixelScan**, which allows the user to select a pixel on a spectral image and obtain the CL spectrum at that pixel, and **ModeViewerNMF**, which performs NMF on the hyperspectral dataset based on a user-specified number of components. After the appropriate intensity filtering, the IHV reveals that the Ag nanocube supports three distinct plasmon modes: a corner mode, an edge mode, and a bulk mode. Each of these modes is associated with a spectrum in Fig. 3.

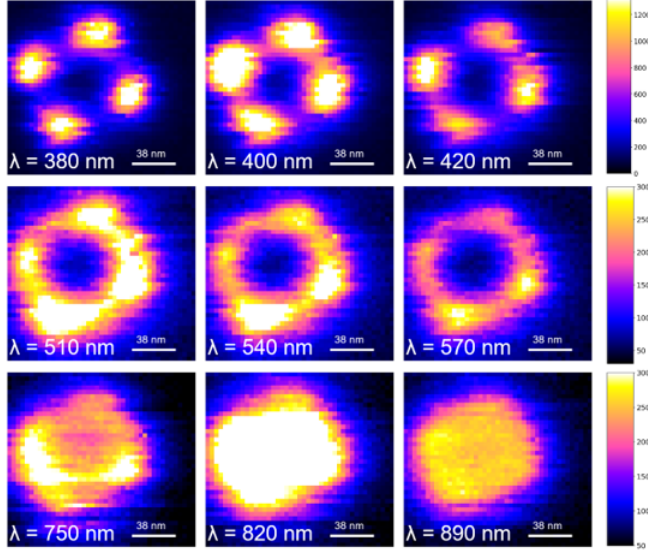


FIG. 4. CL images of localized plasmonic modes in Ag nanocube on ZnO spacer layer

We applied NMF using different n to ensure that all modes could be decomposed. Shown in Fig. 5 are several endmembers and abundance maps obtained by using NMF with $n = 20$. The corner, edge, and bulk modes are captured within the first five components, and the corresponding endmember features are consistent with the spectrum shown in Fig. 3. However, a majority of the remaining seem to exhibit processes that are either noise-dominated or cannot be captured by NMF. It is important to note here that NMF is a purely mathematical decomposition and cannot distinguish objectively between a weak signal and noise.⁹

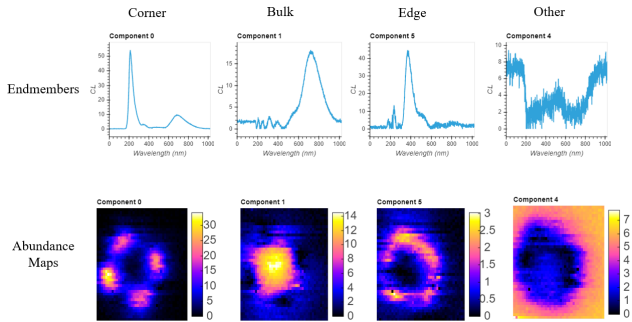


FIG. 5. NMF components depicting corner, edge, and bulk modes

Incident electrons from the CL electron beam perturb the

density of conduction electrons in the impinging region. The perturbation and the electron charge behave as a dipole oriented normal to the surface, serving as a source of surface plasmon polaritons (SPP). The SPP's propagate toward the Ag nanocube and decouple as they scatter from it. The broadband transition radiation (TR) produced by the impinging electrons traveling at relativistic speeds will interact with the SPP since they are mutually coherent, thus producing interference that is detected in the far field.¹⁸

CL images of the Ag nanocube are collected at a wider field of view these interference patterns. Using the IHV, we generate interferograms over the wavelength range from 444 nm to 884 nm, revealing the interaction between the SPP's and the transition radiation. From these interferograms, information about the characteristic phase of the scattered radiation can be extracted. In a previous study on spherical Ag nanoparticles coupled to a metallic substrate conducted by Sannomiya et al.,¹⁹ the constructive interference condition between SPP's and transition radiation as a function of radial distance R along the substrate surface from a nanoparticle on the substrate is described by,

$$R = \frac{\Phi_{osc} + 2m\pi}{k_{spp} + k \sin(\theta) \cos(\phi)} \quad (2)$$

where Φ_{osc} is the phase of the field scattered by the particle, m is an integer, k_{spp} is the SPP wave vector, k is the free-space light vector, ϕ is the in-plane azimuthal angle relative to the defined x axis, and Δ is the additional phase delay associated with the interaction distance of the SPP with the sphere. This can be seen by drawing a linescan by scanning radially outward from the nanocube at the center of the interferograms to the bottom right corner. A Savitzky-Golay filter was applied to the linescan (not shown) to clean out the noise by fitting the curve with higher order polynomials over consecutive local regions on a given spectrum. Further analysis of the radial dependence of the SPP/transition radiation interference is currently underway.

V. CONCLUSION

We have applied and studied NMF to two distinct datasets: a multidimensional Raman dataset on the QSL candidate α -RuCl₃, and a hyperspectral CL dataset on an Ag nanopatch antenna. We wrote a Python library for conducting NMF on the Raman dataset and used it to perform exploratory data analysis. We found, based on an analysis of the NMF reconstruction error, that $n = 4$ components is adequate for capturing the information contained in a dataset. For the Ag nanopatch antenna, we developed the IHV tool, which allows the user to interactively visualize hyperspectral CL data. Using the IHV, we resolved corner, edge, and bulk localized plasmonic modes and extract the spectra associated with these regions on the Ag nanocube. Adapting NMF functions from the α -RuCl₃, we decomposed the hyperspectral data, validating these spectra with the endmembers and abundance maps. Finally, we used the IHV to visualize the interference of propagating SPP's with transition radiation.

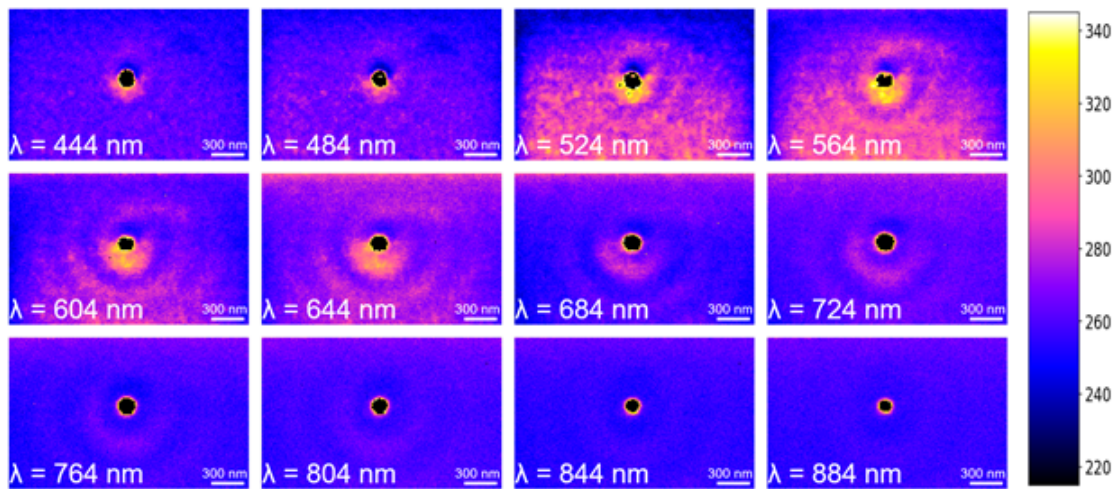


FIG. 6. Interferograms depicting SPP and transition radiation interference. Each image is taken at an interval of 40 nm, with a bandwidth of 4 nm.

Future efforts in data visualization will be focused on adapting pan sharpening, a technique which fuses a panchromatic image with a hyperspectral or multispectral image to produce a resultant image with both high spatial resolution and high spectral fidelity. While there are many different algorithms for performing pan sharpening, a method called coupled NMF has been particularly promising for materials datasets.^{9,20} By building on the NMF we have presented in this paper and applying it to the pan sharpening context, we seek to improve the quality of CL images. On the data analysis front, there we seek to expand our analysis techniques to methods such as Variational Auto Encoders (VAE), which may be able to capture some of the nonlinear processes exhibited in our plasmonic datasets that cannot be captured by NMF, which is an inherently linear decomposition.

ACKNOWLEDGMENTS

This work was supported in part by the U.S. Department of Energy, Office of Science, Office of Workforce Development for Teachers and Scientists (WDTS) under the Science Undergraduate Laboratory Internships (SULI) program. A portion of this research was conducted at the Center for Nanophase Materials Sciences, which is a DOE Office of Science User Facility. Author Yoong Sheng Phang would like to thank his SULI mentor Dr. Ben Lawrie for his guidance and for the incredible opportunity to work on this project, postdoctoral researchers Vasudevan Iyer and Yun-Yi Pai for their mentorship and suggestions on computational data analysis, and fellow SULI intern Brian Lerner for his insights with Python.

VI. REFERENCES

- ¹S. Somnath, C. R. Smith, S. Jesse, and N. Laanait, “Pycroscopy - an open source approach to microscopy and microanalysis in the age of big data and open science,” *Microscopy and Microanalysis* **23**, 224–225 (2017).
- ²S. Somnath, C. R. Smith, N. Laanait, R. K. Vasudevan, and S. Jesse, “Usid and pycroscopy – open source frameworks for storing and analyzing imaging and spectroscopy data,” *Microscopy and Microanalysis* **25**, 220–221 (2019).
- ³L. Loncan, L. B. de Almeida, J. M. Bioucas-Dias, X. Briottet, J. Chanussot, N. Dobigeon, S. Fabre, W. Liao, G. A. Licciardi, M. Simoes, J.-Y. Tourneret, M. A. Veganzones, G. Vivone, Q. Wei, and N. Yokoya, “Hyperspectral pansharpening: A review,” *IEEE Geoscience and Remote Sensing Magazine* **3**, 27–46 (2015).
- ⁴N. J. Schilder, H. Agrawal, E. C. Garnett, and A. Polman, “Phase-resolved surface plasmon scattering probed by cathodoluminescence holography,” *ACS Photonics* **7**, 1476–1482 (2020).
- ⁵N. Gillis, “The why and how of nonnegative matrix factorization,” *Regularization, Optimization, Kernels, and Support Vector Machines* **12** (2014).
- ⁶P. Sajda, S. Du, and L. Parra, *Recovery of constituent spectra using non-negative matrix factorization*, Optical Science and Technology, SPIE’s 48th Annual Meeting, Vol. 5207 (SPIE, 2003).
- ⁷A. N. Srivastava, B. Matthews, and S. Das, “Algorithms for spectral decomposition with applications to optical plume anomaly detection,”.
- ⁸J. Röhm, *Non-Negative Matrix Factorization for Raman Data Spectral Analysis*, Thesis (2017).
- ⁹N. Borodinov, P. Banerjee, S. H. Cho, D. J. Milliron, O. S. Ovchinnikova, R. K. Vasudevan, and J. A. Hachtel, “Enhancing hyperspectral eels analysis of complex plasmonic nanostructures with pan-sharpening,” *J Chem Phys* **154**, 014202 (2021).
- ¹⁰L. Savary and L. Balents, “Quantum spin liquids: a review,” *Rep Prog Phys* **80**, 016502 (2017).
- ¹¹J. Wen, S.-L. Yu, S. Li, W. Yu, and J.-X. Li, “Experimental identification of quantum spin liquids,” *npj Quantum Materials* **4** (2019), 10.1038/s41535-019-0151-6.
- ¹²A. Kitaev, “Anyons in an exactly solved model and beyond,” *Annals of Physics* **321**, 2–111 (2006).
- ¹³M. Ziatdinov, A. Banerjee, A. Maksov, T. Berlijn, W. Zhou, H. B. Cao, J. Q. Yan, C. A. Bridges, D. G. Mandrus, S. E. Nagler, A. P. Baddorf, and S. V. Kalinin, “Atomic-scale observation of structural and electronic orders in the layered compound -rucl₃,” *Nature Communications* **7**, 13774 (2016).
- ¹⁴S. Y. Park, S. H. Do, K. Y. Choi, D. Jang, T. H. Jang, J. Schefer, C. M. Wu, J. S. Gardner, J. M. S. Park, J. H. Park, and S. Ji, “Emergence of the isotropic kitaev honeycomb lattice with two-dimensional ising universality in α -rucl₃,” (2016), arXiv:1609.05690 [cond-mat.mtrl-sci].
- ¹⁵L. J. Sandilands, Y. Tian, K. W. Plumb, Y. J. Kim, and K. S. Burch, “Scattering continuum and possible fractionalized excitations in α -rucl₃,” *Phys Rev Lett* **114**, 147201 (2015).
- ¹⁶D. Wulferding, Y. Choi, S. H. Do, C. H. Lee, P. Lemmens, C. Faugeras,

- Y. Gallais, and K. Y. Choi, “Magnon bound states versus anyonic majorana excitations in the kitaev honeycomb magnet $\alpha\text{-RuCl}_3$,” *Nat Commun* **11**, 1603 (2020).
- ¹⁷S. He, W. Zhang, L. Liu, Y. Huang, J. He, W. Xie, P. Wu, and C. Du, “Baseline correction for raman spectra using an improved asymmetric least squares method,” *Anal. Methods* **6**, 4402–4407 (2014).
- ¹⁸M. Kuttge, E. J. R. Vesseur, A. F. Koenderink, H. J. Lezec, H. A. Atwater, F. J. García de Abajo, and A. Polman, “Local density of states, spectrum, and far-field interference of surface plasmon polaritons probed by cathodoluminescence,” *Physical Review B* **79** (2009), 10.1103/PhysRevB.79.113405.
- ¹⁹T. Sannomiya, A. Konecna, T. Matsukata, Z. Thollar, T. Okamoto, F. J. Garcia de Abajo, and N. Yamamoto, “Cathodoluminescence phase extraction of the coupling between nanoparticles and surface plasmon polaritons,” *Nano Lett* **20**, 592–598 (2020).
- ²⁰N. Yokoya, T. Yairi, and A. Iwasaki, “Coupled non-negative matrix factorization (cnmf) for hyperspectral and multispectral data fusion: Application to pasture classification,” (2011) pp. 1779–1782.